arXiv:1601.07347v1 [quant-ph] 27 Jan 2016

Deterministic Generation of Multiparticle Entanglement by Quantum Zeno Dynamics

Giovanni Barontini[1], Leander Hohmann[1], Florian Haas[1,2], Jérôme Estève[1] & Jakob Reichel[1*]

[1]Laboratoire Kastler Brossel, ENS, UPMC-Paris 6, CNRS, Collège de France, 24 rue Lhomond, 75005 Paris, France

[2]Present address: TWS-Partners AG, 80538 München, Germany

[*]To whom correspondence should be addressed; E-mail: jakob.reichel@ens.fr

January 28, 2016

Multiparticle entangled quantum states, a key resource in quantum-enhanced metrology and computing, are usually generated by coherent operations exclusively. However, powerful new forms of quantum dynamics can be obtained when environment coupling is used as part of the state generation. Here we demonstrate the use of Quantum Zeno Dynamics (QZD), based on non-destructive measurement with an optical microcavity, to deterministically generate different multi-particle entangled states in an ensemble of 36 qubit atoms in less than $5\,\mu$s. We characterize the resulting states by performing quantum tomography, yielding a time-resolved account of the entanglement generation. We study the dependence on measurement strength, and quantify the depth of entanglement. These results show that QZD is a versatile tool for fast and deterministic entanglement generation in quantum engineering applications.

Engineering a desired quantum state – including the increasingly complex entangled states required for quantum computing and quantum simulations – is usually accomplished using coherent interactions exclusively, such as a resonant field driving an atomic transition. Recent developments show that measurement and environment coupling can also be used as powerful tools for quantum engineering [1, 2, 3, 4, 5, 6, 7]. One intriguing example is Quantum Zeno Dynamics (QZD), which has been theoretically studied for more than a decade [8, 9, 10].

QZD combines a coherent interaction with a measurement that is applied simultaneously. In the simplest case, this measurement detects just a single, initially unoccupied state in the large state space in which the system evolves. If the measurement is performed frequently enough, measurement backaction will keep the detected state unoccupied indefinitely – this is the well-known quantum Zeno effect. However, the simple fact of blocking one state also entails a profound modification of the dynamics elsewhere in the state space: this dynamics, called QZD, remains coherent, but produces states that can be completely different from those produced by the same coherent interaction without the measurement [8, 9, 10]. Indeed, QZD may result in quantum states that would be inaccessible in the absence of measurement, and which are potentially interesting for quantum engineering. The experimental challenge is to realize the required non-demolition measurement, which must have high efficiency for one state (or a group of states) without affecting the fragile quantum coherences in the rest of the state space. Single-particle QZD has been performed by inducing losses on a specific atomic state [11]. Other recent experiments with single Rydberg atoms [12] and photons in a superconducting microwave cavity [13] have used unitary operators to divide the state space and thus obtain an equivalent effect without the use of measurement.

Here we use a cavity-based measurement in the regime of high cooperativity, $C \gg 1$, where $C = g^2/2\kappa\gamma$, g is the single-atom coupling rate to the cavity field and κ and γ are the atomic and cavity half-linewidths at half maximum. Compared to other forms of optical detection, the cavity reduces the spontaneous emission rate by orders of magnitude, making this a good approximation of an ideal projective measurement [14, 15, 16]. An ensemble of ^{87}Rb atoms is confined in a single antinode of the cavity field, ensuring a near-identical coupling rate $g = 2\pi \times 190\,\mathrm{MHz}$. Two hyperfine ground state sublevels serve as qubit states $|0\rangle$ and $|1\rangle$ (Fig. 1A); a microwave source is used to drive transitions between these states, realizing a unitary operation U_{MW}. Because the cavity and microwave fields both provide near-identical coupling to all the atoms, the relevant Hilbert space consists of the symmetric states of the collective atomic spin, which is spanned by the Dicke states $|n_N\rangle$ (Fig. 1B), where n is the number of atoms in $|1\rangle$ and N is the total atom number [16]. In our experiment, cavity and probe beam are tuned as shown in Fig. 1A, so that the measurement distinguishes the state $|0_N\rangle$ (all atoms in $|0\rangle$), for which the cavity transmits, from the subspace Z of all other states, for which it reflects [15]. When U_{MW} takes the N-atom state close to the boundary of Z, the dynamics in presence of the measurement strongly differs from U_{MW} applied alone. The resulting states are highly entangled in general, and their purity depends on the measurement being strong enough and at the same time sufficiently nondestructive. For example, starting from the initial state $|N_N\rangle$ (all atoms in $|1\rangle$), driving microwave Rabi oscillations with Rabi frequency Ω (trajectory I in Fig. 1C) would normally produce the state $|0_N\rangle$ after an evolution time $T = \pi/\Omega$. If the cavity measurement is applied simultaneously with the microwave drive, however, the system cannot reach this state. Instead, it evolves through a state which is very close to the W state, $|1_N\rangle = 1/\sqrt{N}(|10\ldots0\rangle + |010\ldots0\rangle + \ldots + |00\ldots1\rangle)$, an entangled state which is robust against particle loss and enables some metrological gain over nonentangled states [17, 18]. If instead the microwave drive follows trajectory II in Fig. 1C, such that U_{MW}

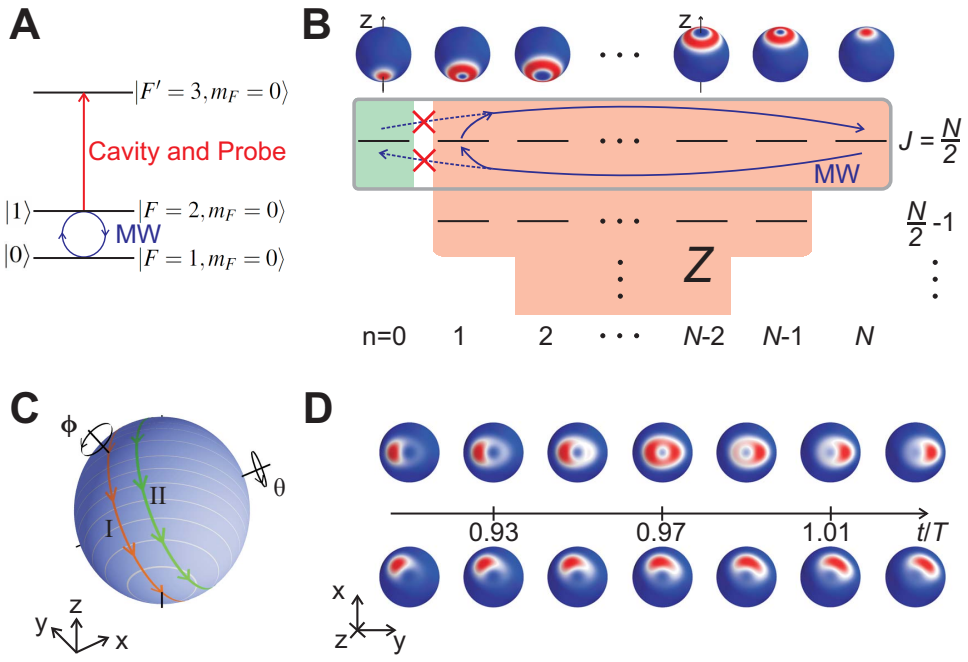

Figure 1: **Quantum Zeno dynamics of atoms coupled to a cavity.** (**A**) Relevant level scheme of ^{87}Rb. A resonant 6.8 GHz microwave allows applying arbitrary rotations to the atomic qubit. Cavity and probe laser are resonant with the transition $|1\rangle \rightarrow |F'=3,m_{F'}=0\rangle$. The cavity transmits only when the atoms are in the $|0_N\rangle$ state. (**B**) The Hilbert space of the symmetric atomic spin states is spanned by the Dicke states $|n_N\rangle$ (see text). The Husimi-Q distributions of some of these states are also displayed. Starting with the atoms in $|N_N\rangle$, we apply the microwave and simultaneously measure cavity transmission, leading to coherent evolution that is restricted to the subspace Z (orange shaded area). (**C**) Microwave excitations used in the experiment. Plotted are the Bloch sphere trajectories of the mean spin without measurement. Trajectory I drives the mean spin through the south pole while trajectory II avoids the pole. (**D**) Simulated evolution of the Husimi-Q distribution on the Bloch sphere for 36 atoms on trajectory I (upper row) and trajectory II (lower row) under cavity measurement.

would go through a state different from but close to $|0_N\rangle$, then a different entangled state is obtained. Fig. 1D shows simulated Husimi-Q distributions of the atoms for the two trajectories in presence of measurement, in the vicinity of the π-pulse time.

In the experiment, we use an ensemble of 36 ± 2 atoms [16]. In order to track the dynamics, we take snapshots of the atomic state by stopping the microwave and the measurement at different times t during the evolution. For each t, we measure $Q(\theta,\phi)$ [15, 16] of the resulting state. In the absence of measurement, driving the atoms along trajectory I, we obtain the usual Rabi oscillation (Fig. 2A, upper panel). By contrast, in the presence of measurement, we observe that the Husimi-Q distribution is deformed and features the expected dip in the center (lower panel in Fig. 2A) when the state reaches the south pole. Figs. 2B and C show the result of full 2D tomography for different times on trajectories I and II. In both cases, as the state approaches

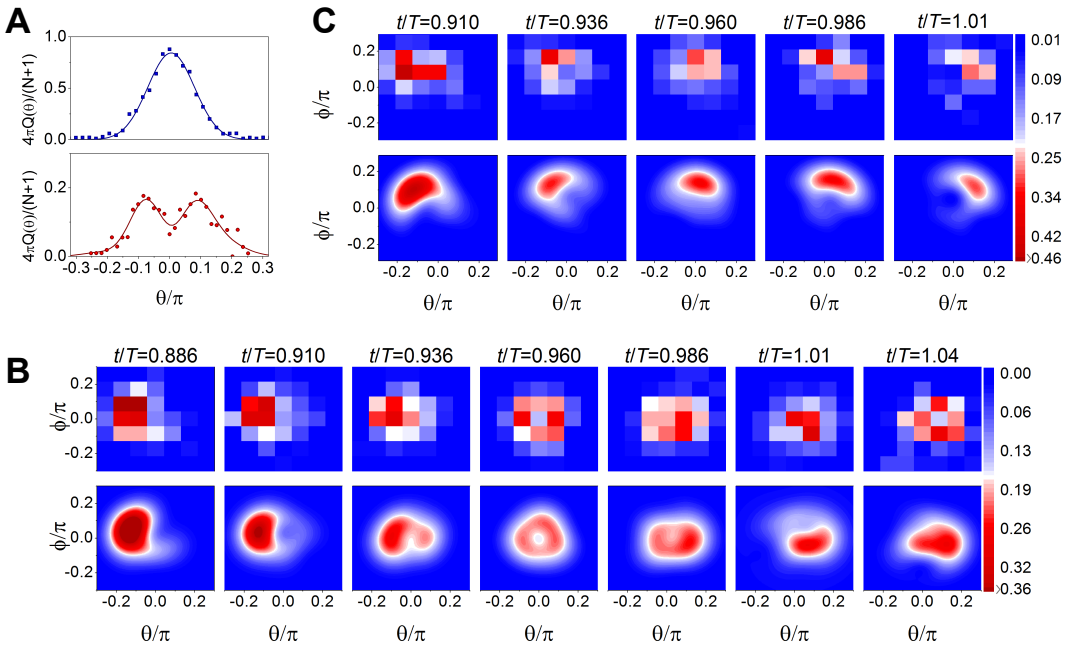

Figure 2: **Tomography of quantum Zeno dynamics.** (**A**) Measured high-resolution 1d cuts of the Husimi-Q distributions $Q(\theta, \phi = 0)$ when the mean spin reaches the south pole. The upper panel shows the state after microwave drive along trajectory I without measurement. The Husimi-Q function displays the $\cos(\theta/2)^N$ dependence of the coherent state. The lower panel results from the same microwave drive, but in the presence of measurement. The Husimi-Q function shows a characteristic dip. The lines are maximum-likelihood reconstructions [16]. (**B**) Measured 2d distributions $Q(\theta, \phi)$ at different times for trajectory I in presence of measurement. The 7×7 measurement grid is centered around the south pole. The lower row shows the Husimi-Q distribution corresponding to the reconstructed density matrices. For $t/T = 0.96$, a ring-shaped distribution appears, indicating high overlap with the W state. (**C**) Same as (B), but for trajectory II. The quantum Fisher information normalized to the initial atom number $N = 36$ is, from left to right, $1.51^{+0.39}_{-0.08} 1.25^{+0.3}_{-0.17} 1.47^{+0.14}_{-0.42} 1.19^{+0.25}_{-0.14} 1.14^{+0.25}_{-0.11}$. The measurement rate is $r_\mathrm{m} \simeq 22.5\,\Omega$ for all panels.

the boundary of Z, its Q function is deformed such that $Q(0, 0)$, which is proportional to the population in $|0_N\rangle$, remains small at all times. Driving the dynamics further, the state recovers its gaussian character as it leaves the measurement boundary.

From the tomographic measurements, we reconstruct the symmetric part ρ_s of the atomic ensemble density matrix ρ using a maximum likelihood method [15, 16]. On trajectory I, the Q function completely encircles the forbidden state for $t = 0.96\,T$, where $T = 4.65\,\mu$s. At this time, the population ρ_{11} of the W state reaches a maximum of 0.37 ± 0.04, while $\rho_{00} = 0.17 \pm 0.03$. Knowing ρ_{11} and ρ_{00}, we can use the entanglement depth criterion derived in [15]: any N-particle ρ that has a given combination $\{\rho_{00}, \rho_{11}\}$, when decomposed into smaller density matrices $\rho_1 \otimes \ldots \otimes \rho_M$, must contain at least one ρ_i with $\dim \rho_i \geq k$, where k depends on the values $\{\rho_{00}, \rho_{11}\}$. Thus, this criterion gives the minimum number of atoms

that are demonstrably entangled with one another, but makes no statement about the strength of this entanglement, which might be weak. Such a criterion of k-particle entanglement – which does not involve the exact knowledge of ρ_i – was first derived for spin-squeezed states [19]. Our $k(\rho_{00}, \rho_{11})$, derived in [15], efficiently detects entanglement in the vicinity of the W state. Applied to the state for $t/T = 0.96$, it reveals that this state contains at least 8^{+3}_{-5} entangled particles, in spite of the experimental imperfections discussed below.

For trajectory II, the resulting distributions are compressed in one direction with respect to a coherent state. For such states, our entanglement depth criterion is not efficient. To assess their nonclassical character, we calculate a lower bound on their quantum Fisher information F_{Q} [18, 16]. For ideal QZD (infinite measurement rate and no loss) on this trajectory, numerical simulations indicate a maximum $F_{\mathrm{Q}}/N \simeq 3.4$ reached for $t/T \simeq 0.96$. It has been shown that $F_{\mathrm{Q}} > N$ is a sufficient (but not necessary) condition for entanglement; also, F_{Q}/N is the maximum achievable reduction in the variance of an estimate of a quantum phase using that state, with respect to the shot noise limit [18, 20]. The experimentally realized states in Fig. 2C yield $F_{\mathrm{Q}}/N = \{1.51, 1.25, 1.47, 1.19, 1.14\}$ [16], showing that this trajectory too, creates states that are entangled and feature some metrological gain with respect to classical states.

The cavity measurement is characterized by an effective rate which is not infinitely high, and is accompanied by spontaneous emission, which tends to populate undesired states outside the symmetric subspace. Experimentally, the symmetric subspace population $\mathrm{Tr}\,\rho_s$ is readily available from the reconstructed density matrices. Fig. 3A shows the decay of $\mathrm{Tr}\,\rho_s$ for trajectory I. A model [16] including spontaneous emission (solid line), with no adjustable parameters, reproduces the data well. Apart from this decay, the features of the QZD can be understood without taking spontaneous emission into account. Figs. 3B,C show the measured relative populations $\rho'_{ii} = \rho_{ii}/\,\mathrm{Tr}\,\rho_s$ (filled symbols), comparing them to ideal QZD (dot-dashed lines) and QZD with finite measurement rate (dashed lines). ρ'_{00}, which would reach 1 in the absence of measurement, is strongly reduced by the measurement (Fig. 3B), while ρ'_{11} is increased (Fig. 3C). We also observe that the turning point of the Rabi oscillation of the collective spin shifts to shorter times (Fig. 3D), which is expected because the measurement reduces the dimension of the Hilbert space. The deviation from the ideal QZD is well described by a simpler model (dashed lines), which takes into account only the finite measurement rate, but not the spontaneous emission. The atoms coherently evolve according to the hamiltonian $H_{\mathrm{MW}}/\hbar = \Omega J_x$ and are subject to quantum jumps with a single jump operator $d = \sqrt{r_{\mathrm{m}}}\,|0_N\rangle\,\langle 0_N|$ accounting for the effect of the measurement [16]. The measurement rate is $r_{\mathrm{m}} = 2\Phi\sqrt{T_0}$, where Φ is the photon flux entering the cavity and T_0 the empty-cavity transmission [14]. The dashed lines are calculated for $r_{\mathrm{m}}/\Omega = 22.5$, the value expected from the measured photon flux incident onto the cavity, $\Phi = 21 \times 10^6\ \mathrm{s}^{-1}$. The full model including spontaneous emission (solid lines) gives very similar predictions for ρ'_{ii}.

For a given cavity, higher Φ increases the measurement rate and thus reduces the contamination of the state by $|0_N\rangle$. However, it also increases the spontaneous emission rate and thus the contamination by states outside the symmetric subspace. The optimum measurement rate is a compromise between these conflicting effects. We have investigated this by varying Φ as

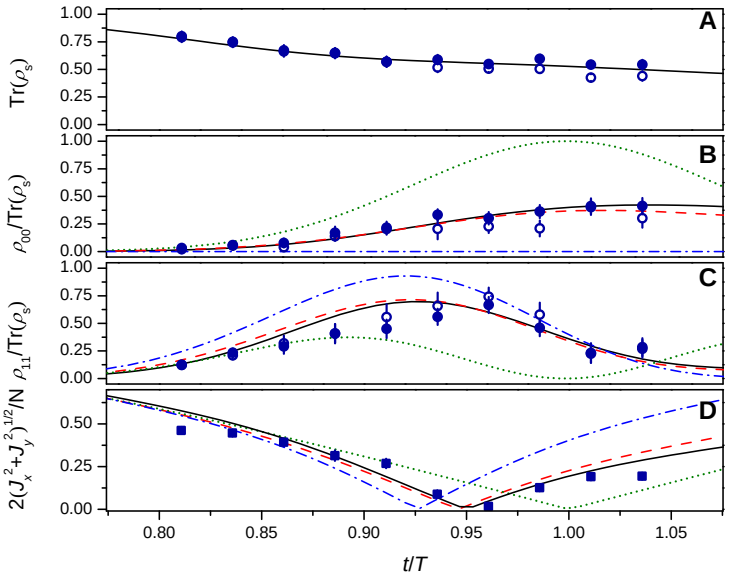

Figure 3: **Evolution of the Dicke state populations during QZD along trajectory I.** The measured populations (filled symbols) are deduced from the data in Fig. 2B. (**A**) Population inside the symmetric subspace. (**B**), (**C**) Relative populations of the Dicke states $|0_N\rangle$ (B) and $|1_N\rangle$ (C). (**D**) Transverse spin length $2/N\sqrt{J_x^2+J_y^2}$, where J_i is the i-th component of the collective atomic spin. For comparison, green dotted lines in (B)-(D) show the expected evolution without measurement (Rabi oscillation). The measured data is well described by a model including spontenous emission [16] with no adjustable parameters (black solid lines). The dynamics within the symmetric subspace can also be understood neglecting spontaneous emission (red dashed lines). Blue dot-dashed lines are predictions for ideal QZD ($r_\mathrm{m} \to \infty$). Open symbols: measured evolution excluding runs with nonzero cavity transmission during the QZD. Error bars are 1σ statistical errors of the reconstruction.

shown in Fig. 4. By solving the full model described above, we obtain the solid curves in Fig. 4, which are in good agreement with the experimental data, and which show a broad maximum of ρ_{11} as a function of r_m. The data in Fig. 2B is taken at $r_\mathrm{m} = 22.5\,\Omega$, which maximizes the number of entangled particles as deduced from the criterion [15].

By detecting transmitted photons on a photodetector behind the cavity, we can access the result of the Zeno measurement, i.e., obtain information about whether the dynamics was indeed restricted to Z. This additional information can be exploited to improve the fidelity of the produced state, at the price of excluding some data. In the data of Fig. 2, a transmitted photon is observed for 5-17% of the runs, depending on t. Excluding these runs from the analysis indeed improves the quality of resulting state, as shown by the open symbols in Fig. 3 and 4. As an example, for trajectory I at $t = 0.96\,T$, we obtain an entanglement depth of 11^{+2}_{-3} atoms.

The state fidelity can be improved drastically with a better cavity, using technology that is already available today. In our cavity, mirror birefringence causes a second, orthogonally

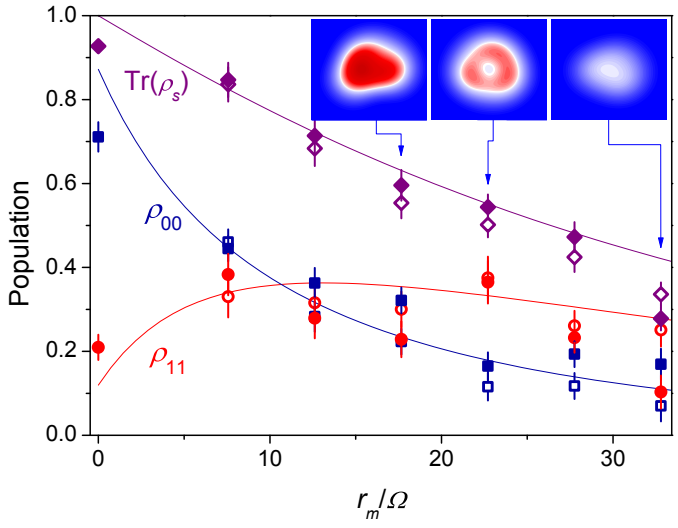

Figure 4: **QZD for different measurement strengths.** Tomography measurements are taken after a fixed evolution time $t = 0.96\,T$ for different measurement rates (see text), using trajectory I. Filled symbols: reconstructed ρ_{00} (blue squares) and ρ_{11} (red circles), and population in the symmetric subspace (purple diamonds). Solid lines: results of the full model. The insets show some of the reconstructed Husimi-Q distributions. Increasing the effective measurement rate from zero, ρ_{00} decreases while ρ_{11} increases as normal dynamics turns into QZD. At the same time, spontaneous emission increases, reducing the population in the symmetric subspace. Open symbols: runs with nonzero cavity transmission excluded.

polarized TEM00 mode located at a detuning of 540 MHz from the probed mode. This makes the spontaneous emission rate much larger than in a birefringence-free cavity with the same linewidth and g. In the latter, the spontaneous emission rate for atoms in $|n_N\rangle$ is $r_{\rm m}/(2nC)$ for $n \geq 1$ [14]. For our cavity and transition, the atomic and cavity half-linewidths at half maximum are $\gamma = 2\pi \times 3\,$MHz and $\kappa = 2\pi \times 53\,$MHz, so that $C \simeq 100$. Fiber cavities have been fabricated recently with a finesse approaching 200000 [21, 22, 23] (instead of 37000 in our cavity) and with a birefringence reduced to zero [23]. With these improvements alone and all other parameters unchanged, we calculate a state fidelity $\rho_{11} \simeq 0.8$.

These results demonstrate that QZD is an experimentally feasible tool for quantum engineering of multiparticle systems. So far, many QZD proposals have focused on two-qubit systems [24, 25, 26, 27, 28, 29]. It appears promising to explore extensions of the scheme studied here. For example, combining driven Rabi oscillations with a non-demolition measurement on the equator of the Bloch sphere [30, 31] could lead to highly entangled states in the vicinity of the measurement boundary, similar to the mechanism proposed for photons in [10].

References and Notes

[1] F. Verstraete, M. M. Wolf, and J. I. Cirac. *Quantum computation and quantum-state engineering driven by dissipation.* Nat. Phys., **5**, 633 (2009). 1745-2473.

[2] I. D. Leroux, M. H. Schleier-Smith, and V. Vuletić. *Implementation of Cavity Squeezing of a Collective Atomic Spin*. Phys. Rev. Lett., **104**, 073602 (2010).

[3] J. T. Barreiro, M. Muller, P. Schindler, D. Nigg, T. Monz, M. Chwalla, M. Hennrich, C. F. Roos, P. Zoller, and R. Blatt. *An open-system quantum simulator with trapped ions*. Nature, **470**, 486 (2011). 0028-0836.

[4] H. Krauter, C. A. Muschik, K. Jensen, W. Wasilewski, J. M. Petersen, J. I. Cirac, and E. S. Polzik. *Entanglement Generated by Dissipation and Steady State Entanglement of Two Macroscopic Objects*. Phys. Rev. Lett., **107**, 080503 (2011).

[5] S. Shankar, M. Hatridge, Z. Leghtas, K. M. Sliwa, A. Narla, U. Vool, S. M. Girvin, L. Frunzio, M. Mirrahimi, and M. H. Devoret. *Autonomously stabilized entanglement between two superconducting quantum bits*. Nature, **504**, 419 (2013). 0028-0836.

[6] Y. Lin, J. P. Gaebler, F. Reiter, T. R. Tan, R. Bowler, A. S. Sorensen, D. Leibfried, and D. J. Wineland. *Dissipative production of a maximally entangled steady state of two quantum bits*. Nature, **504**, 415 (2013).

[7] R. McConnell, H. Zhang, J. Hu, S. Cuk, and V. Vuletić. *Entanglement with negative Wigner function of almost 3000 atoms heralded by one photon*. Nature, **519**, 439 (2015).

[8] P. Facchi and S. Pascazio. *Quantum Zeno Subspaces*. Phys. Rev. Lett., **89**, 080401. doi: \bibinfo{doi}{10.1103/PhysRevLett.89.080401} (2002).

[9] P. Facchi and S. Pascazio. *Quantum Zeno dynamics: mathematical and physical aspects*. J. Phys. A: Math. Theor., **41**, 493001 (2008).

[10] J. M. Raimond, C. Sayrin, S. Gleyzes, I. Dotsenko, M. Brune, S. Haroche, P. Facchi, and S. Pascazio. *Phase Space Tweezers for Tailoring Cavity Fields by Quantum Zeno Dynamics*. Phys. Rev. Lett., **105**, 213601 (2010).

[11] F. Schäfer, I. Herrera, S. Cherukatti, C. Lovecchio, F. S. Cataliotti, F. Caruso, and A. Smerzi. *Experimental realization of quantum Zeno dynamics*. Nat. Commun., **5**, 3194 (2014).

[12] A. Signoles, A. Facon, D. Grosso, I. Dotsenko, S. Haroche, J.-M. Raimond, M. Brune, and S. Gleyzes. *Confined quantum Zeno dynamics of a watched atomic arrow*. Nat. Phys., **10**, 715 (2014).

[13] L. Bretheau, P. Campagne-Ibarcq, E. Flurin, F. Mallet, and B. Huard. *Quantum dynamics of an electromagnetic mode that cannot contain N photons*. Science, **348**, 776 (2015).

[14] J. Volz, R. Gehr, G. Dubois, J. Estève, and J. Reichel. *Measurement of the internal state of a single atom without energy exchange*. Nature, **475**, 210 (2011).

[15] F. Haas, J. Volz, R. Gehr, J. Reichel, and J. Estève. *Entangled States of more Than 40 Atoms in an Optical Fiber Cavity*. Science, **344**, 180 (2014).

[16] See Materials and Methods.

[17] W. Dür, G. Vidal, and J. I. Cirac. *Three qubits can be entangled in two inequivalent ways*. Phys. Rev. A, **62**, 062314. doi:\bibinfo{doi}{10.1103/PhysRevA.62.062314} (2000). URL `http://link.aps.org/doi/10.1103/PhysRevA.62.062314`.

[18] L. Pezze and A. Smerzi. *Entanglement, Nonlinear Dynamics, and the Heisenberg Limit*. Phys. Rev. Lett., **102**, 100401 (2009).

[19] A. S. Sørensen and K. Mølmer. *Entanglement and extreme spin squeezing*. Phys. Rev. Lett., **86**, 4431 (2001).

[20] H. Strobel, W. Muessel, D. Linnemann, T. Zibold, D. B. Hume, L. Pezzé, A. Smerzi, and M. K. Oberthaler. *Fisher information and entanglement of non-Gaussian spin states*. Science, **345**, 424 (2014).

[21] A. Muller, E. B. Flagg, J. R. Lawall, and G. S. Solomon. *Ultrahigh-finesse, low-mode-volume Fabry–Perot microcavity*. Opt. Lett., **35**, 2293. doi:\bibinfo{doi}{10.1364/OL.35.002293} (2010).

[22] B. Brandstätter, A. McClung, K. Schuppert, B. Casabone, K. Friebe, A. Stute, P. O. Schmidt, C. Deutsch, J. Reichel, R. Blatt, and T. E. Northup. *Integrated fiber-mirror ion trap for strong ion-cavity coupling*. Rev. Sci. Instrum., **84**, 123104 (2013).

[23] M. Uphoff, M. Brekenfeld, G. Rempe, and S. Ritter. *Frequency splitting of polarization eigenmodes in microscopic Fabry-Perot cavities*. New J. Phys., **17**, 013053 (2015). arXiv:1408.4367.

[24] X. B. Wang, J. Q. You, and F. Nori. *Quantum entanglement via two-qubit quantum Zeno dynamics*. Phys. Rev. A, **77**, 062339 (2008).

[25] S. Maniscalco, F. Francica, R. L. Zaffino, N. Lo Gullo, and F. Plastina. *Protecting Entanglement via the Quantum Zeno Effect*. Phys. Rev. Lett., **100**, 090503 (2008).

[26] R. Rossi, K. M. Fonseca Romero, and M. C. Nemes. *Semiclassical dynamics from Zeno-like measurements*. Phys. Lett. A, **374**, 158 (2009).

[27] X. Q. Shao, L. Chen, S. Zhang, and K.-H. Yeon. *Fast CNOT gate via quantum Zeno dynamics*. J. Phys. B, **42**, 165507 (2009).

[28] C. M. Chandrashekar. *Zeno subspace in quantum-walk dynamics*. Phys. Rev. A, **82**, 052108 (2010).

[29] Z. Shi, Y. Xia, W. H.Z., and J. Song. *One-step preparation of three-particle Greenberger-Horne-Zeilinger state via quantum Zeno dynamics*. Eur. Phys. J. D, **66**, 127 (2012).

[30] M. H. Schleier-Smith, I. D. Leroux, and V. Vuletić. *States of an Ensemble of Two-Level Atoms with Reduced Quantum Uncertainty*. Phys. Rev. Lett., **104**, 073604. doi:\bibinfo{doi}{10.1103/PhysRevLett.104.073604} (2010). URL http://link.aps.org/doi/10.1103/PhysRevLett.104.073604.

[31] J. Appel, P. J. Windpassinger, D. Oblak, U. B. Hoff, N. Kjærgaard, and E. S. Polzik. *Mesoscopic atomic entanglement for precision measurements beyond the standard quantum limit*. Proc. Natl. Acad. Sci. U.S.A., **106**, 10960 (2009).

[32] S. Kuhr, W. Alt, D. Schrader, I. Dotsenko, Y. Miroshnychenko, A. Rauschenbeutel, and D. Meschede. *Analysis of dephasing mechanisms in a standing-wave dipole trap*. Phys. Rev. A, **72**, 023406 (2005).

[33] L. M. K. Vandersypen and I. L. Chuang. *NMR techniques for quantum control and computation*. Rev. Mod. Phys., **76**, 1037 (2005).

[34] R. Gehr, J. Volz, G. Dubois, T. Steinmetz, Y. Colombe, B. L. Lev, R. Long, J. Estève, and J. Reichel. *Cavity-Based Single Atom Preparation and High-Fidelity Hyperfine State Readout*. Phys. Rev. Lett., **104**, 203602. doi:\bibinfo{doi}{10.1103/PhysRevLett.104.203602} (2010).

[35] J. Rehacek, Z. Hradil, and M. Jezek. *Iterative algorithm for reconstruction of entangled states*. Phys. Rev. A, **63**, 040303 (2001). URL http://link.aps.org/doi/10.1103/PhysRevA.63.040303.

[36] D. Petz and C. Ghinea. *Introduction to quantum Fisher information*. In *Quantum Probability and Related Topics*, volume 1, 261–281 (2011).

[37] G. Tóth and I. Apellaniz. *Quantum metrology from a quantum information science perspective*. Journal of Physics A: Mathematical and Theoretical, **47**, 424006 (2014).

[38] P. Facchi, G. Marmo, and S. Pascazio. *Quantum Zeno dynamics and quantum Zeno subspaces*. In *Journal of Physics: Conference Series*, volume 196, 012017. IOP Publishing (2009).

Acknowledgements: This work was supported by the European Union Information and Communication Technologies project QIBEC (Quantum Interferometry with Bose-Einstein Condensates) (GA 284584) and by the Institut Francilien pour la Recherche sur les Atomes Froids (IFRAF). We thank Jürgen Volz, Roger Gehr and Guilhem Dubois for their contributions to early stages of this experiment.

Author contributions: G. B. and L. H. performed the experiment; F. H. contributed to setting it up. G. B., L. H., J. E. and J. R. contributed to data analysis and interpretation, as well as to the manuscript.

Supplementary Materials:

Materials and Methods
Figs. S1 – S7
Table S1
References (32–38)

Materials and Methods

Atom chip and fiber Fabry-Perot cavity

The experimental setup consists of an atom chip for the production of ultracold trapped ^{87}Rb atomic samples, integrated with a high finesse fiber Fabry-Perot cavity. The experimental procedure to produce the cold sample and transfer it to the optical trap in the cavity has been described in [14]. The sample is loaded into a single antinode of a 830 nm standing wave dipole trap inside the cavity. The cavity has a length of $39\,\mu$m, estimated radii of curvature of the mirrors of $450\,\mu$m and $150\,\mu$m, and a finesse of 37000. Parameters of the coupled atom-cavity system are $(\kappa, \gamma, g) = 2\pi \times (53, 3, 190)$ MHz. In contrast to previous experiments where the atomic cloud was placed at the geometrical center of the cavity, here we load the atoms at the waist of the 780 nm probe laser which is located $8\,\mu$m from the input mirror (which has the larger radius of curvature). This leads to a 10% enhancement of our atom-cavity coupling with respect to previous experiments. Due to birefringence in the mirrors, our cavity features two orthogonally polarised eigenmodes with a frequency splitting of 540 MHz [14, 23]. In the present experiments, probe and dipole beams are coupled to the higher-frequency cavity mode. An external magnetic bias field of 12.5 G is oriented parallel to this mode, thus both lasers are π-polarised (Fig.). To reduce the effect of ambient magnetic fields, we implement our atomic qubit in the states $\{|0\rangle \equiv |F = 1, m_F = 0\rangle, |1\rangle \equiv |F = 2, m_F = 0\rangle\}$ which are insensitive to magnetic field fluctuations. The probe laser is tuned close to resonance with the $|1\rangle \rightarrow |F' = 3, m_F = 0\rangle$ transition of the D2 line of ^{87}Rb.

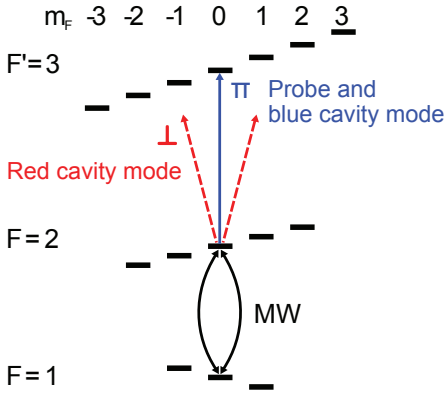

Fig. S1:
Relevant levels of ^{87}Rb. A magnetic field is applied along the polarization direction of the blue cavity mode (see text), which is also the polarization of the probe beam.

The measurements performed in [15] indicated that the coherence time of the final entangled state was mainly limited by the temperature of the sample [32]. Due to an improved laser-cooling setup and optimisation of the cavity locking apparatus, we now prepare atomic samples at a temperature of 50μK (about 10 times colder than in [15]), which increases the coherence time by one order of magnitude. We expect the temperature of the atomic ensemble to contribute

only negligibly to decoherence in the present experiment. Additionally, the delay between the preparation of the entangled state and the tomography in the present experiment is only $14\,\mu$s.

Atom number preparation and experimental sequence

The atoms magnetically trapped by the atom chip are initially in the $|F = 2, m_F = 2\rangle$ state. Once loaded in the cavity dipole trap, we transfer them to $|0\rangle$ by means of three consecutive microwave sweeps. In $F = 1$, the atoms are not resonant with the light field in the cavity, thereby acting as a dispersive medium with each atom shifting the cavity resonance by $6\,$MHz. In order to prepare a sample with precise atom number, we send probe light into the cavity for a long time, causing atom losses via light-assisted collisions (see [15]). By simultaneously monitoring the cavity transmission, we can infer the number of atoms left in the cavity and switch off the probe beam when the desired value is reached. We terminate the preparation sequence with a weak measurement pulse to check for faulty sample preparation (atoms in $|1\rangle$ at $t = 0$, 25% of runs).

The atom preparation process has a low probability to populate the other Zeeman sub-levels of the $F = 1$ manifold. However, atoms in these sub-levels do not participate in any of the following steps; in particular, they do not contribute to the tomography measurement because they are not resonant with the microwave pulses. We verified the atom number in $|0\rangle$ after the preparation from a separate tomography measurement of the initial state, as shown in the upper panel of Fig. 2A. In the present experiments, we prepared a target number of 40 atoms in $F = 1$ and measured the number of atoms in the cavity that are in the correct Zeeman sub-state to be 36 ± 2. This control measurement was repeated periodically to exclude drifts in the atom number.

Once the atoms are prepared in the desired state, we start one of the trajectories I and II, followed by state tomography, as shown in Fig. **S2**. Initially, all the atoms are in $|0\rangle$ so that the total spin points to the south pole of the Bloch sphere. The QZD sequence itself should start with a state fully inside Z. The most basic protocol would therefore consist in first applying a π pulse to get from $|0_N\rangle$ to $|1_N\rangle$ and then a $\theta = -\pi t/T$ pulse, accompanied by cavity measurement to perform the Zeno dynamics. However, it is crucial for the production of the W state (Fig. 2A and 2B) to use a trajectory that passes exactly through the south pole. Therefore, to realize trajectory I starting from $|0_N\rangle$, we first perform a $\theta = 2\pi$ pulse, then a $-\pi$ pulse immediately followed by the $\theta = -\pi t/T$ pulse accompanied by measurement. It has been shown that this pulse sequence compensates for both pulse length and detuning fluctuations [33], ensuring that the trajectory in the absence of measurement passes exactly through the south pole of the Bloch sphere. To perform trajectory II, starting with all atoms in $|0\rangle$, we first apply a small rotation around the Y axis (for the experiment shown in Fig. 2C $\phi = \pi/10$) and then a $\theta = \pi$ rotation followed by the $\theta = \pi t/T$ rotation accompanied by the probing of the cavity.

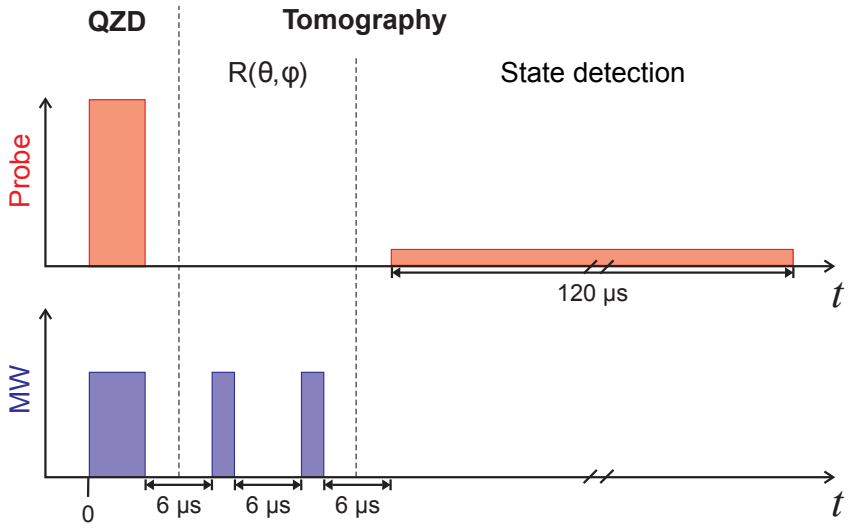

Fig. S2: **Timing sequence of QZD and tomography.** The coherent microwave pulse with simultaneous detection constitutes the actual quantum Zeno dynamics. Its duration is variable, but is typically close to the π-pulse duration $T = 4.65\,\mu$s. Then follows the state tomography, which consists of a state rotation realized by two microwave pulses, and a detection pulse. The delay of $6\,\mu$s between any two pulses is imposed by hardware restrictions.

Cavity measurement

The cavity measurement uses the method described previously in [14, 15]. Note that it is robust with respect to variations in the coupling rate: in order to keep the atoms indistinguishable during measurement, the only requirement is to realize high cooperativity $C \gg 1$ for each participating atom. Any atom in that regime will cause the required binary cavity response – full transmission for $|0\rangle$, full reflection for $|1\rangle$, and thus, the measurement will not distinguish different atoms by their coupling rates. The fulfillment of this requirement is experimentally confirmed by the fact that we do not observe intermediate values of transmission. (We can deliberately create them by strongly heating the atom cloud.)

Tomographic measurement

Immediately after the QZD we perform the 2D state tomography. Given the atomic ensemble density matrix ρ, our tomography method [15] measures the quantity

$$P_0(\theta, \phi) = \langle 0_N | R^\dagger(\theta, \phi) \rho R(\theta, \phi) | 0_N \rangle \,,$$

where $R(\theta, \phi)$ is a microwave rotation and ρ is the density matrix of the N atomic qubits. The dimension of the corresponding Hilbert space is 2^N. However, because $P_0(\theta, \phi)$ is always 0 for states outside the symmetric subspace (i.e., total spin $J < N/2$, see figure 1) [15], our

measurement only yields information about the symmetric part of the density matrix state $\rho_s = \Pi\rho\Pi$, where Π is the projector on the subspace of states with $J = N/2$ that are symmetric under particle exchange. The dimension of this subspace is $N+1$. The Husimi-Q distribution of ρ_s is defined as $Q(\theta,\phi) = \frac{N+1}{4\pi} P_0(\theta,\phi)$ and contains all the information about ρ_s. In particular, the total probability of being in the symmetric subspace $\mathrm{Tr}\,\rho_s$ is given by the integral of Q.
For one complete 2D tomography measurement, we scan the tomography angles θ (around X) and ϕ (around Y) each between $-0.26\pi, ..., 0.26\pi$, resulting in a 7x7 grid of individual measurements at different (θ,ϕ). To perform the required rotation $R(\theta,\phi)$, we apply two consecutive microwave pulses, with adjustable durations (0.4...1.2 μs here) and phases; for technical reasons, there is a delay of 6 μs between successive pulses leading to a total time delay of 14 μs between preparation and tomography. We then probe the cavity during 120 μs and measure the transmitted and reflected photon counts on avalanche photodiodes (APDs), from which we decide if the cavity transmission was high or low (see [34] for more details). The experimental sequence is repeated in order to get at least 50 measurements for each tomography angle, from which we deduce $P_0(\theta,\phi)$ as the frequency of high transmission events. The measurement of $P_0(\theta,\phi)$ is subject to the detection errors $\epsilon_{01}(\epsilon_{10})$ corresponding to the probability to measure a high cavity transmission when there is in reality at least one atom in $F = 2$ (a low cavity transmission when in reality all atoms are in $F = 1$). The errors ϵ_{01} and ϵ_{10} are computed as described in [15] and depend on the average time for one atom to change its hyperfine state. These lifetimes vary with the relative population of the two hyperfine states which in turn depend on the tomography angle. We estimate the lifetimes independently for each tomography angle to calculate $\epsilon_{01}(\theta,\phi)$ and $\epsilon_{10}(\theta,\phi)$. In all measurements they are below 6%.

Maximum likelihood reconstruction of the density matrix

Given our measurement results for $P_0(\theta,\phi)$, we reconstruct the symmetric part of the density matrix, ρ_s, including its off-diagonal elements, in the Dicke state basis $\{|n_N\rangle\}$. We use the maximum-likelihood algorithm described in [35]. Starting from an arbitrary initial density matrix, we iteratively find the matrix that maximizes the likelihood of producing the observed results, taking into account the detection errors $\epsilon_{01}(\theta,\phi)$ and $\epsilon_{10}(\theta,\phi)$ of the tomographic measurement. We use the experimetally measured atom number N. Varying it on the scale of the experimental uncertainty produces no significant variation in the reconstruction results. Including too few basis states prevents the reconstruction from correctly reproducing the experimental data while including too many states increases the noise without giving additional information. As can be seen in Table **S1**, the reconstructed populations do not change when we include Dicke states with $n > 4$ and we therefore truncate the basis to the first fifth Dicke states ($0 \leq n \leq 4$) for all presented data. Fig. **S3** shows the evolution of all five populations during QZD. From the reconstructed 5×5 density matrix, we can calculate the Husimi-Q function for arbitrary angle and produce the high resolution density plots shown in Figure 2.
To estimate the statistical error on the quantities that we infer from the reconstructed density matrix, we use a bootstrapping method. We generate sets of artificial measurements each having

a)	ρ_{00}	ρ_{11}	ρ_{22}	ρ_{33}	ρ_{44}	ρ_{55}	ρ_{66}	$\mathrm{Tr}(\rho_s)$
$n_{\max}=2$	0.16	0.38	0.01					0.55
$n_{\max}=3$	0.17	0.36	0.01	0.01				0.55
$n_{\max}=4$	0.17	0.36	0.01	0.00	0.01			0.55
$n_{\max}=5$	0.17	0.36	0.01	0.00	0.00	0.00		0.55
$n_{\max}=6$	0.17	0.36	0.01	0.00	0.00	0.00	0.00	0.55
b)	ρ_{00}	ρ_{11}	ρ_{22}	ρ_{33}	ρ_{44}	ρ_{55}	ρ_{66}	$\mathrm{Tr}(\rho_s)$
$n_{\max}=2$	0.03	0.13	0.22					0.38
$n_{\max}=3$	0.03	0.08	0.15	0.15				0.40
$n_{\max}=4$	0.02	0.07	0.11	0.12	0.08			0.41
$n_{\max}=5$	0.03	0.05	0.12	0.13	0.07	0.01		0.40
$n_{\max}=6$	0.02	0.07	0.12	0.11	0.07	0.01	0.01	0.41

Table S1: **Reconstructed density matrix populations ρ_{ii} for different basis truncations.** The basis includes the Dicke states with $0, 1, \ldots, n_{\max}$ atoms in $|1\rangle$. (a) Reconstructed populations for the state in Fig. 2B obtained after a QZD of $t/T = 0.96$. (b) The same reconstruction but for the state displayed in the rightmost frame of Fig. 2C.

the same number of samples and the same average $P_0(\theta, \phi)$ as the experimental data. For each 2D tomography measurement, we then operate the reconstruction algorithm on 1000 artificial datasets and calculate the quantity of interest in order to obtain its standard deviation. We apply this method to obtain statistical error bars for the populations shown in figures 3,4 and for the quantum Fisher information.

Criteria for multiparticle entanglement

To assess the creation of multiparticle entanglement during QZD, we use two different criteria for the states obtained following trajectory I and II. In the vicinity of the W-state (trajectory I), we employ the criterion described in [15] that gives a lower bound on the entanglement depth of the atomic ensemble based on the populations ρ_{00} and ρ_{11}. For the states created along trajectory II, we compute a lower bound for the quantum Fisher information F_{Q}.

Establishing a lower bound on the quantum Fisher information

We now show that $F_{\mathrm{Q}}(\rho) \geq F_{\mathrm{Q}}(\rho_s)$, and that computing the quantum Fisher information in the symmetric subspace gives us a lower bound for $F_{\mathrm{Q}}(\rho)$. We consider the completely positive, trace preserving map M which transforms ρ into $M[\rho] = \Pi\rho\Pi + \bar{\Pi}\rho\bar{\Pi}$, where Π is defined as before and $\bar{\Pi} = \mathbf{1} - \Pi$. Under a rotation of the atomic spin along the direction $\mathbf{n}$ by an angle θ, ρ transforms into $\rho(\theta)$. The quantum Fisher information associated to the measurement of the angle θ, which we denote by $F_{\mathrm{Q}}(\{\rho(\theta)\})$, cannot increase under the action of M [36] and $F_{\mathrm{Q}}(\{\rho(\theta)\}) \geq F_{\mathrm{Q}}(\{M[\rho(\theta)]\})$. Because the norm of the atomic spin is conserved by

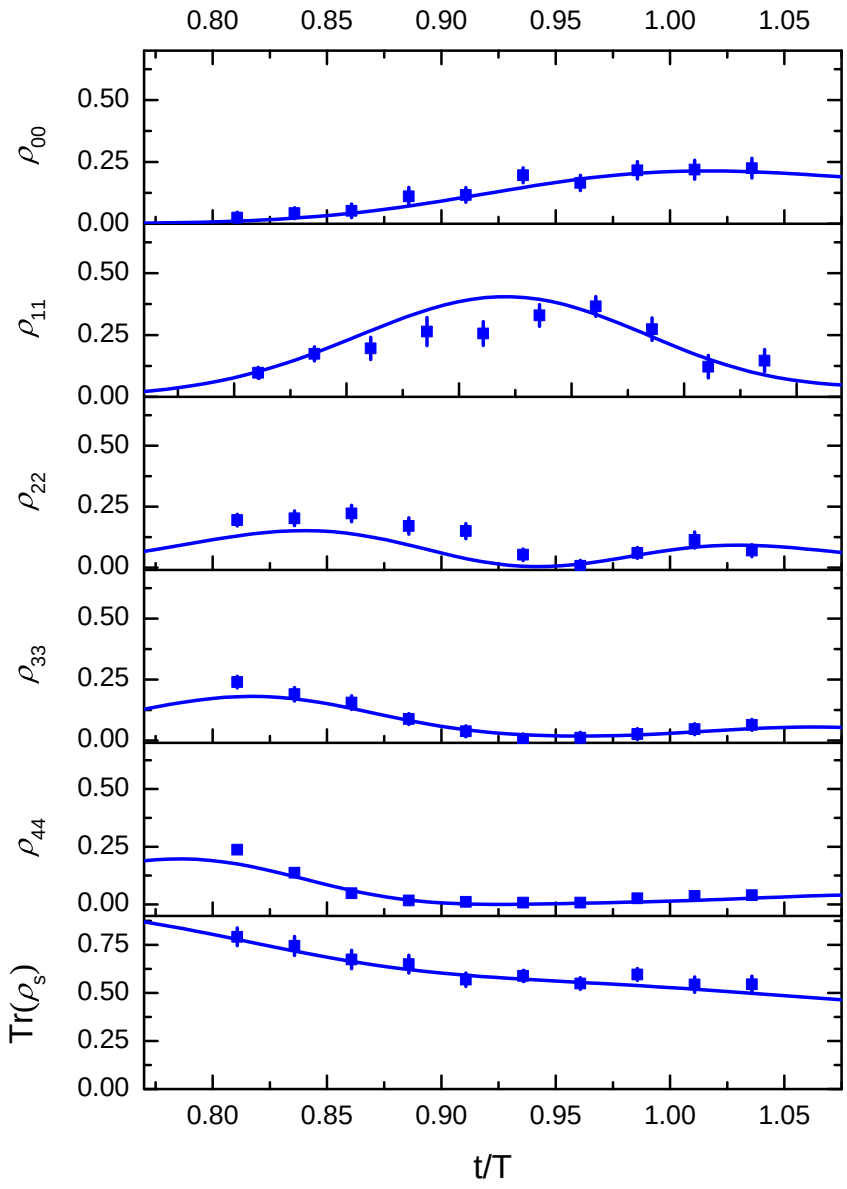

Fig. S3: **Evolution of the populations during QZD along trajectory I.** The points are the populations ρ_{ii}, with $i < 5$, reconstructed from the tomography measurement shown in Fig. 2B. The lowest curve shows the total population in the symmetric subspace. The solid lines are the prediction of Eq. S3.

rotations, we have $M[\rho(\theta)] = \rho_s(\theta)+\rho_{ns}(\theta)$, where $\rho_s(\theta)$ and $\rho_{ns}(\theta)$ are respectively the rotated symmetric part of the density matrix ρ_s and the rotated non-symmetric part of the density matrix $\rho_{ns} = \bar{\Pi}\rho\bar{\Pi}$. We thus conclude that

$$F_{\mathrm{Q}}(\{\rho(\theta)\}) \geq F_{\mathrm{Q}}(\{\rho_s(\theta) + \rho_{ns}(\theta)\}) = F_{\mathrm{Q}}(\{\rho_s(\theta)\}) + F_{\mathrm{Q}}(\{\rho_{ns}(\theta)\}),$$

where the last equality comes from the additivity of the quantum Fisher information under direct sum [37].

Computation of F_{Q}

We compute $F_{\mathrm{Q}}(\rho_s)$ by numerically finding the optimal rotation axis $\mathbf{n}$ that maximizes the corresponding quantum Fisher information $F_{\mathrm{Q}}(\{\rho_s(\theta)\}) = 2\sum_{j,k} \frac{(p_j-p_k)^2}{p_j+p_k}|\langle j|J_{\mathbf{n}}|k\rangle|^2$, where the p_j and $|j\rangle$ are the eigenvalues and eigenvectors of ρ_s. As a consistency check, we have also computed $F_{\mathrm{Q}}(\rho_s)$ for nominally nonentangled states in the experiment. We find $F_Q = 38.7^{+6.8}_{-2.2}$ for the first state ($r_m = 0$) in Fig. 4. In order to estimate our error on $F_{\mathrm{Q}}(\rho_s)$, we use the bootstrapping method as previously described. The errors indicated in the main text correspond to a 68% confidence interval. The lower and upper errors are different because the probability distribution that we deduce from the bootstrapping method is slightly asymmetric. Extended Data Fig. **S4** shows the evolution of $F_{\mathrm{Q}}(\rho_s)$ along the trajectory II with 68% and 95% confidence intervals. Note that $F_{\mathrm{Q}}(\rho_s)$ is a very conservative estimate of the lower bound of $F_{\mathrm{Q}}(\rho)$ because it assumes $F_{\mathrm{Q}}(\rho_{ns}) = 0$. Although we cannot give a precise value to $F_{\mathrm{Q}}(\rho_{ns})$ from our measurements, we can estimate it to be on the order of $(N - n_{\mathrm{sp}})\,\mathrm{Tr}\,\rho_{ns}$. Here, we have simply considered that the n_{sp} spontaneous emission events that lead to a population $\mathrm{Tr}\,\rho_{ns}$ outside the symmetric subspace correspond to a loss of n_{sp} atoms outside the qubit subspace and that the remaining $N - n_{\mathrm{sp}}$ atoms are left in $|0\rangle$. Including this contribution to our estimate of the lower bound for F_{Q} would increase it by approximately 25%.

Modeling the Quantum Zeno Dynamics

Quantum Zeno Dynamics is most often described in terms of repeated projective measurements that are regularly spaced in time with intervals of unitary evolution in between. In our case, the measurement and the unitary evolution are simultaneous and continuous processes. As shown in [38], the expected dynamics are physically equivalent in both cases and tend towards a unitary evolution confined to the degenerate subspace of the measurement in the limit where the measurement rate tends to infinity (*cf.* dash-dotted lines in Fig. 3). Because our measurement is continuous, a natural description of our system is obtained following a master equation approach. Without spontaneous emission, the evolution of the atomic density matrix ρ is given by

$$\frac{d\rho}{dt} = \frac{1}{i\hbar}[H_{\mathrm{MW}}, \rho] + d\rho d^\dagger - \frac{1}{2}\rho d^\dagger d - \frac{1}{2}d^\dagger d\rho\,. \tag{S1}$$

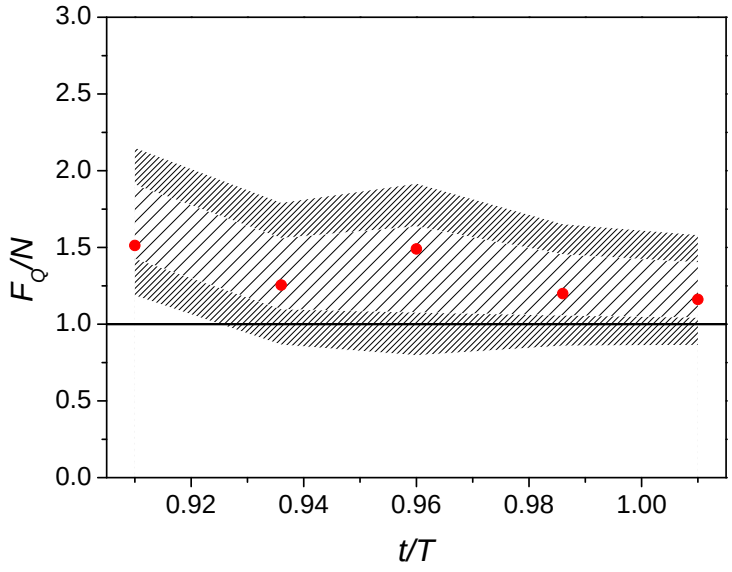

Fig. S4: **Evolution of the quantum Fisher information during QZD along trajectory II.** We estimate a lower bound to the quantum Fisher information $F_{\rm Q}$ of the atomic state by computing $F_{\rm Q}$ of ρ_s that we reconstruct from our tomography measurements. A ratio $F_{\rm Q}/N > 1$ indicates an entangled state. The hatched areas are confidence intervals corresponding to 68% and 95% probabilities. The probability that the first point corresponds to an entangled state with $F_{\rm Q}/N > 1$ is above 99%. For the four other points, this probability is above 90%.

The first term describes the unitary evolution due to the microwave field with $H_{\rm MW}/\hbar = \Omega J_x$. The last three terms account for the effect of the measurement by the cavity in the Lindblad form. Here we consider that light only enters the cavity when the atoms are in $|0_N\rangle$, therefore the loss of a photon from the cavity is described by a jump operator for the atoms that projects them onto $|0_N\rangle$. The probability per unit time of such a jump is $2\kappa\, n_{\rm ph}$ where $n_{\rm ph} = \Phi\sqrt{T_0}/\kappa$ is the average photon number in the cavity when the atoms are in $|0_N\rangle$. The expression of the atom jump operator is thus

$$d = \sqrt{2\kappa\, n_{\rm ph}}|0_N\rangle\langle 0_N| = \sqrt{r_m}|0_N\rangle\langle 0_N|\,, \tag{S2}$$

where $r_m \equiv 2\Phi\sqrt{T_0}$ is the effective measurement rate of the cavity. The populations shown as dashed lines in Fig. 2 are obtained by numerically solving $(S1)$ for the photon flux used in the experiment. This simple model reproduces well the evolution of the atomic state inside the symmetric subspace but cannot account for the decay of the population in this subspace.

Effect of spontaneous emission

Spontaneous emission tends to populate undesired states outside the symmetric subspace. For example, when $|1_N\rangle$ is optically excited, it can emit to $|J = N/2 - 1, n = 1\rangle$. In order to take into account the effect of spontaneous emission and calculate the expected decay of the population in the symmetric subspace, we consider an anti-Hermitian operator $\bar{H}_{\rm loss}$ and the modified master equation

$$\frac{d\rho}{dt} = \frac{1}{i\hbar}[H_{\rm MW}, \rho] + \frac{1}{i\hbar}\{\bar{H}_{\rm loss}, \rho\} + d\rho d^\dagger - \frac{1}{2}\rho d^\dagger d - \frac{1}{2}d^\dagger d\rho\,. \tag{S3}$$

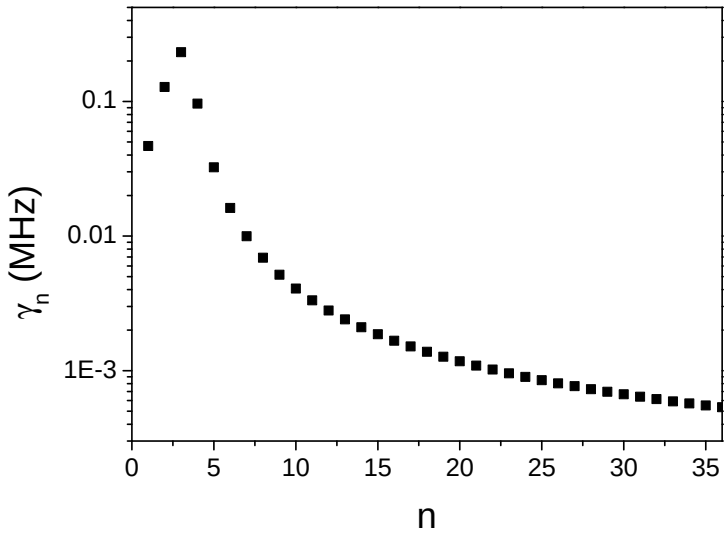

Fig. S5: **Effective loss rate.** Calculated effective loss rates γ_n when the atoms are in state $|n_N\rangle$.

We suppose that $\bar{H}_{\rm loss}$ is diagonal in the Dicke state basis with matrix elements given by $\langle n_N|\bar{H}_{\rm loss}|n_N\rangle = -i\gamma_n$ where $\gamma_n = \gamma\, p_{e,n}$ and $p_{e,n}$ is the probability for one atom among the n atoms in $|1\rangle$ to be optically exited. Here, we neglect the probability ($\sim 1/N$) to fall back into the symmetric subspace after a spontaneous emission. The probability of excitation $p_{e,n}$ is calculated independently from the steady state solution of the atom-cavity master equation describing the coupling of n atoms to the TEM_{00} mode taking into account all known experimental parameters for our setup (magnetic field, lattice depth, ...) as in [14], and in particular the presence of the orthogonally polarized TEM_{00} cavity mode. Fig. **S5** shows the calculated rates γ_n as a function of n corresponding to the photon flux used to measure the data shown in Fig. 2. We then numerically solve (S3) and obtain the populations shown as solid lines in Figs. 3 and 4. The calculated number of spontaneous emission events during the QZD explains the observed decay of the population $\mathrm{Tr}\,\rho_s$ in the symmetric subspace. Fig. **S6** shows 1D tomography measurements for evolution times spanning a larger interval than in the main text. The observed reduction in amplitude of the measured curves is also well explained by our model. Finally, Fig. **S7** shows the expected Husimi-Q distributions obtained from the model and compares them to the ones computed from the reconstructed density matrices.

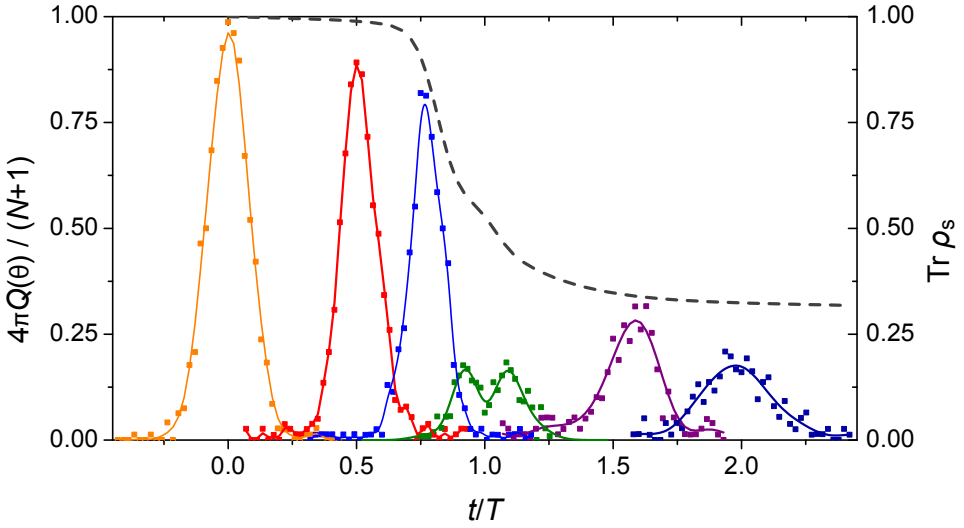

Fig. S6: **Long time evolution of the Husimi-Q distribution during QZD.** Each colored curve corresponds to a 1D measurement of the Husimi-Q distribution for a different evolution time along trajectory I. Solid lines are guides to the eye. For times shorter than the π pulse time (orange, red, blue data), we observe the rotation of the initial coherent state on the Bloch sphere. In the vicinity of the π pulse (green data), the state is strongly modified due to QZD. For larger times (purple, dark blue data), the state recovers a gaussian like shape, but with a reduced amplitude compared to an ideal coherent state. This is due to the effect of spontaneous emission, which leads to a decrease of the population in the symmetric subspace. The dashed gray line shows the evolution of the symmetric subspace population expected from the full model.

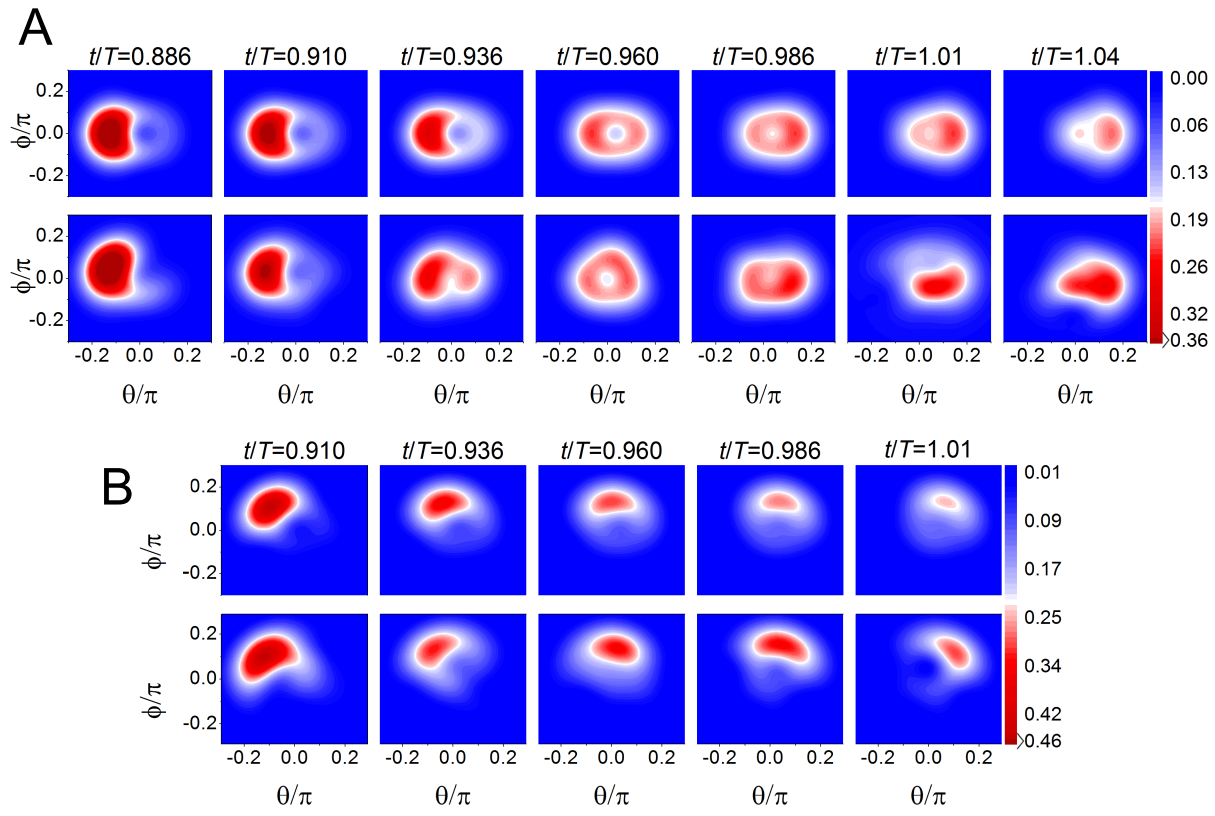

Fig. S7: **Predictions of the full model.** Comparison of the predicted Husimi-Q distributions calculated from the full model including spontaneous emission (upper rows) to the experimentally obtained distributions (lower rows, same as in Fig. 2 in the main text). Panel A (B) corresponds to the trajectory I (II).